IEEE Access
Multidisciplinary : Rapid Review : Open Access Journal

Received March 5, 2019, accepted March 9, 2019, date of publication March 13, 2019, date of current version April 2, 2019.

Digital Object Identifier 10.1109/ACCESS.2019.2904707

Effects of Inferior Myocardial Infarction Sizes and Sites on Simulated Electrocardiograms Based on a Torso-Heart Model

ZHIPENG CAI[1], JIANQING LI[1,2], KAN LUO[3], BOR-SHYH LIN[4], ZHIGANG WANG[5], XIANGYU ZHANG[1], AND CHENGYU LIU[1]

[1]State Key Laboratory of Bioelectronics, Jiangsu Key Lab of Remote Measurement and Control, School of Instrument Science and Engineering, Southeast University, Nanjing 210096, China
[2]School of Biomedical Engineering and Informatics, Nanjing Medical University, Nanjing 211166, China
[3]School of Information Science and Engineering, Fujian University of Technology, Fuzhou 350118, China
[4]Institute of Imaging and Biomedical Photonics, National Chiao Tung University, Tainan 30010, Taiwan
[5]Institute for Medical Science and Technology, University of Dundee, Dundee DD1 4HN, U.K.

Corresponding authors: Jianqing Li (ljq@seu.edu.cn) and Chengyu Liu (chengyu@seu.edu.cn)

This work was supported in part by the National Natural Science Foundation of China under Grant 61571113, Grant 61601124, and Grant 81871444, in part by the Natural Science Foundation of Jiangsu Province under Grant BE2017735, in part by the Natural Science Foundation of Fujian Province under Grant 2018J01639, in part by the Fundamental Research Funds for the Central Universities under Grant 2242018k1G010, and in part by the Postgraduate Research and Practice Innovation Program of Jiangsu Province under Grant KYCX17_0067.

ABSTRACT Myocardial infarction (MI) is one of the major causes of death. Thus, understanding the underlying mechanisms of MI and its clinical features, especially its relationship with common electrocardiography measurements, is important. Heart modeling provides a possible method to simulate certain heart conditions. In this paper, a refined MI torso-heart model was proposed to explore the effect of inferior MI on simulated electrocardiograms. This model simulated the electrical activity of a normal heart and an inferior MI heart at three sites (basal, middle, and apical) with three MI sizes (small, moderate, and large), aiming to investigate the effect of inferior MI on the simulated electrocardiograms. Simulated body surface potential maps were compared with clinical body surface potential maps to verify the efficiency of the model. A new measure, namely, the *normalized variation coefficient*, was proposed for result evaluation. The results showed that the augmented unipolar left lower limb lead was the best choice for inferior MI diagnoses and it showed the most obvious electrocardiography signal differences between normal and inferior MI hearts. The simulation results corresponded well with commonly used clinical diagnostic criteria. Thus, the proposed refined MI torso-heart model provides a finite element simulation method for quantifying the effects of inferior MI on a torso-heart model-based electrocardiogram and has good potential for use in optimizing electrocardiogram detection.

INDEX TERMS Biomedical engineering, biomedical signal processing, computational modeling, computer simulation, electrocardiography, finite element methods, signal analysis, signal processing.

I. INTRODUCTION

Cardiovascular disease remains a leading cause of death worldwide, accounting for 17.5 million deaths every year [1]. The prevalence of cardiovascular disease in China is on the rise: approximately 3 million deaths are caused by cardiovascular disease annually [2]. Among fatal heart diseases, myocardial infarction (MI) may cause acute death without any prior signs or symptoms [3].

The associate editor coordinating the review of this manuscript and approving it for publication was Gerard-Andre Capolino.

A standard 12-lead electrocardiogram (ECG) is a common method for MI diagnosis, but different MI conditions will lead to different changes in 12-lead ECGs. To investigate certain leads that can better reflect different MIs, a body surface potential map (BSPM) is introduced to provide enhanced spatial resolution [4]. Because the leads are placed on the entire body surface, BSPMs advantageously provide omnidirectional scanning. However, the complexity of the BSPM acquisition process and the difficulty in processing simultaneous signals for numerous channel ECGs limit routine application

2169-3536 © 2019 IEEE. Translations and content mining are permitted for academic research only.
Personal use is also permitted, but republication/redistribution requires IEEE permission.
See http://www.ieee.org/publications_standards/publications/rights/index.html for more information.

to patients with acute MI [5]. However, due to the development of cardiac modeling and simulation [6], the technical complexity of mapping procedures can be avoided by modeling on realistic geometries and using mathematical models.

Several models have been established to investigate the electrical activity and conduction of the heart under normal and abnormal conditions [7]–[9]. These models were constructed using coupling quasi-anatomical geometries (derived from MRI/CT data) [7], [8] and mathematical models of different heart organs (detected from real heart ionic channels) [10], [11]. One representative work, proposed by Sovilj *et al.* [12], was the torso-heart model using an anatomically realistic three-dimensional model geometry and modified FitzHugh-Nagumo equations to simulate whole-heart electrical activity. However, the use of detailed and high-resolution anatomically accurate geometry requires dedicated software and extensive computation times for solving biophysically mathematical models. Therefore, Sovilj *et al.* [13] also presented a simplified three-dimensional cardiac bidomain model to optimize the computational load and model complexity and offered a replicable tool for investigating the effects of MI on a standard 12-lead ECG morphology. Although this model can obtain observable changes between normal and MI ECGs, there remain two limitations: (1) the imposed MI regions are qualitative and cover almost one-third of the ventricle; and (2) the exaggerated MI regions were inconsistent with clinical observations. These two challenges limited the application of this heart-modeling method on refined MI region cases. Therefore, it is extremely important to develop a MI-region-refined model based on clinical observations to investigate detailed changes in MI on simulated ECGs. In this paper, we proposed a refined MI torso-heart model by modifying the heart with detailed MI regions and different sites to study imperceptible changes of quasi-life-size MI on a standard 12-lead ECG morphology. Additionally, up to 308 measuring points were applied on the proposed model to obtain BSPMs. The amplitude changes of five characteristic waves (Q wave, R wave, S wave, ST segment and T wave) were calculated to evaluate the effects of inferior MI (IMI) on simulated ECGs. The results showed that the lead aVF was the most obvious lead that reflected the influence of IMI on body surface ECGs.

II. METHODOLOGY

A. ORIGINAL TORSO-HEART MODEL

The original model is a simplified three-dimensional bidomain torso-heart model, consisting of a torso, lungs and an entire heart (Fig. 1 (a1)), which can simulate 12-lead ECGs under normal and pathological heart states. In this model, the torso, lungs and blood chambers were defined as passive volume conductor regions. The governing equation for the electric potential (V) in the passive volume conductor was given by the Laplace formulation of Maxwell's equations as follows [13]:

$$\nabla \cdot (-\sigma_o \nabla V) = 0 \tag{1}$$

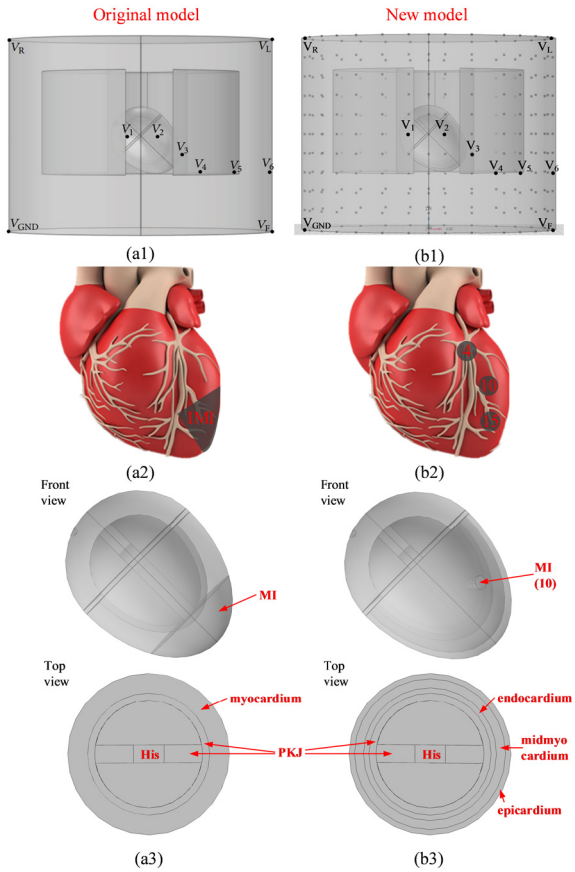

FIGURE 1. A simplified three-dimensional torso-heart model. (a1) The geometry of the original torso-heart model and electrode positions of 12-lead ECGs [13], (a2) the exaggerated IMI region defined in the original model showed on a quasi-real heart [13], (a3) the front view and top view of ventricle in original model [13], (b1) the geometry of the modified MI-region-refined torso-heart model and the 308 additional measuring points containing the electrode positions of 12-lead ECGs, (b2) the refined IMI regions defined in the modified MI-region-refined torso-heart model showed on a quasi-real heart, (b3) the front view and top view of ventricle in modified MI-region-refined torso-heart model.

where σ_o is the electrical conductivity of passive volume conductor, with values given in TABLE 1. All exterior boundaries of the torso were set to be electrically insulating, and all interior boundaries in contact with the heart were set to $V = V_e$, where V_e is the extracellular voltage in the myocardial walls.

The limb leads of the standard 12-lead ECGs were obtained by setting the right and left arms and legs at the corners of the model. The V1-V6 electrodes were located at the anatomical positions of the model. The RL was defined as ground reference. The heart region was divided into seven subdomains according to the anatomical structure of the heart: sinoatrial node, atria, atrioventricular node, His bundle, bundle branches, Purkinje fibers and ventricular myocardium. The mathematical model of the heart tissue was the bidomain model, which was based on the following modified FitzHugh-Nagumo equations [12], [13]:

$$\frac{\partial V_e}{\partial t} - \frac{\partial V_i}{\partial t} + \nabla \cdot (-\sigma_e \nabla V_e) = i_{\text{ion}} \tag{2}$$

TABLE 1. Model parameters and initial values in different regions.

Parameter	Sinoatrial node	Atria	Atrioventricular node	His bundle	bundle branches	Purkinje fibers	Ventricles
a	-0.6	0.13	0.13	0.13	0.13	0.13	0.13
b	-0.3	0	0	0	0	0	0
c_1 ($A \cdot S \cdot V^{-1} m^{-3}$)	1000	2.6	2.6	2.6	2.6	2.6	2.6
c_2 ($A \cdot S \cdot V^{-1} m^{-3}$)	1	1	1	1	1	1	1
d	0	1	1	1	1	1	1
e	0.066	0.0132	0.0132	0.005	0.0022	0.0047	0.006
A (mV)	33	140	140	140	140	140	140
B (mV)	-22	-85	-85	-85	-85	-85	-85
k (s^{-1})	1000	1000	1000	1000	1000	1000	1000
σ_e ($mS \cdot m^{-1}$)	0.5	8	0.5	10	15	35	8
σ_i ($mS \cdot m^{-1}$)	0.5	8	0.5	10	15	35	8
V_i (V)	-0.06	-0.085	-0.085	-0.085	-0.085	-0.085	-0.085
V_e (V)	0	0	0	0	0	0	0
u	0	0	0	0	0	0	0

$$\frac{\partial V_i}{\partial t} - \frac{\partial V_e}{\partial t} + \nabla \cdot (-\sigma_i \nabla V_i) = -i_{\text{ion}} \tag{3}$$

$$\frac{\partial u}{\partial t} = ke\left[\frac{V_m - B}{A} - du - b\right] \tag{4}$$

where V_e represents the extracellular potential, V_i represents the intracellular potential, and u is a recovery variable governing cellular refractoriness. σ_e and σ_i are the extracellular and intracellular conductivities, respectively, $V_m = V_i - V_e$, and a, b, c_1, c_2, d, e, k, A, and B are parameters given in TABLE 1, and i_{ion} is defined as (5) within the sinoatrial node and (6) within the atria, ventricles, atrioventricular node, His bundle, bundle branches and Purkinje fibres.

$$i_{\text{ion}} = kc_1 (V_m - B)\left[a - \frac{V_m - B}{A}\right]\left[1 - \frac{V_m - B}{A}\right] + kc_2 u \tag{5}$$

$$i_{\text{ion}} = kc_1 (V_m - B)\left[a - \frac{V_m - B}{A}\right]\left[1 - \frac{V_m - B}{A}\right] + kc_2 u (V_m - B) \tag{6}$$

The boundary conditions for boundaries contacting the passive volume conductor were zero flux for V_i, and equal to the outward current density from the passive volume conductor for V_e. Additionally, the initial values of V_i, V_e and u are given in TABLE 1. In this model, two kinds of MI were simulated by imposing MI regions at the anterior and inferior walls of the left ventricle (Fig. 1 (a1, a2, a3)) by setting the intracellular conductivity $\sigma_i$and k to zero in the infarcted regions and the initial values to -60 mV and -20 mV for V_i and V_e, respectively. However, the distributions of these two cases did not correspond to standardized myocardial segmentation principles (Fig. 2) [3]. Their MI sizes almost covered the entire lower left ventricle, indicating that the anterior MI covered parts of the apex segment (17), apical lateral segment (16) and apical anterior segment (13), and the IMI covered parts of the apex segment (17), apical lateral segment (16) and apical inferior segment (15). Therefore, based on the standardized myocardial segmentation principle, the MI regions imposed in this model did not fit the definition of anterior MI and IMI.

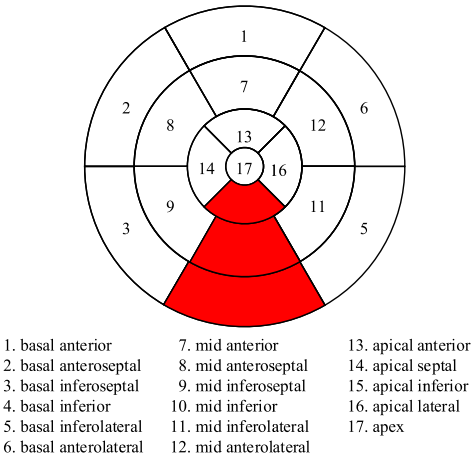

FIGURE 2. The standardized 17 myocardial segments displayed on a circumferential polar plot. The red segments marked the refined IMI sites simulated in this paper [3].

B. MI-REGION-REFINED TORSO-HEART MODEL

Because the aim of this paper was to investigate the effects of MI sizes and sites on simulated ECGs, we did not change the settings of the original MI except for sizes and sites. It is worth noting that single MI is a dominant ischaemia that may cause death, accounting for 79% of visible infarcts in the Rancho/USC database [14]. Therefore, the IMI regions were refined to study the effects of single IMI sizes and sites on ECG morphology (Fig. 1 (b1, b2)). The distribution rule of the single IMI sites followed the standardized myocardial segmentation principle, and the IMI regions (4, 10, 15) were marked as red as shown in Fig. 1 (b2). Each IMI region examined in this paper was located at the center of each segment and had the same parameter settings as in the original model. According to an anatomical study, the size of a single MI in different regions of the left ventricle was divided into

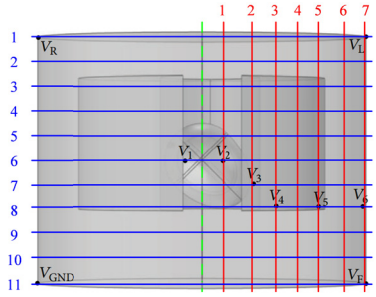

FIGURE 3. The distribution rule of 308 leads on the body surface.

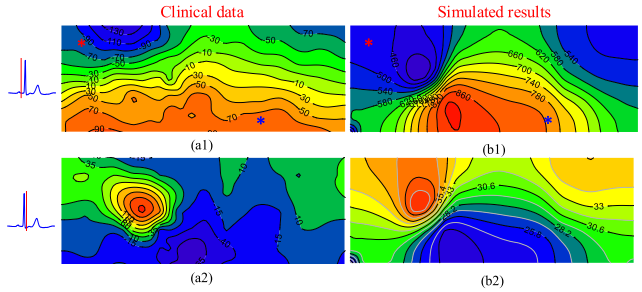

FIGURE 4. Typical BSPMs of two datasets. (a1) and (a2) BSPMs from the clinical data around the heart; (b1) and (b2 BSPMs from the simulated results. The '∗' were the electrode positions of the irregular body surface ECG.

three types: small, moderate and large [15]. In this study, to simplify the geometry of the model, the ventricular wall was divided into three parts, representing the epicardium, the midmyocardium and the endocardium (Fig. 1 (b3)). In the model, an approximate frustum region was used to represent the infarcted myocardium (Fig. 1 (b2)). Small infarcts were only located in the endocardium, whereas moderate infarcts covered the endocardium and midmyocardium, and large infarcts were transmural, spanning the endocardium, midmyocardium and epicardium. The average sizes of the infracted myocardium for small, moderate and large sizes were 100.74 mm^3, 325.43 mm^3 and 490.9 mm^3, respectively. To investigate the BSPMs of the model, 308 leads were added on the surface of the torso. The 308 leads included 11 rows and 28 columns, which were distributed evenly on the surface of the torso (Fig. 1 (b1)). As shown by a red line in Fig. 3, the left anterior ellipse was divided into 7 columns so that V2-V6 could be included in the columns. Therefore, the whole ellipse was separated into 28 columns. Similarly, the whole ellipse was evenly separated into 11 rows. In Fig. 3, blue lines indicate the 11 rows, and a green dotted line is the center of the ellipse. Then, the 12-lead ECGs can be directly derived from the BSPMs. To ensure the results of our MI-region-refined model were comparable to the original model, the model settings (geometry and governing equations) and the electrode positions of the standard 12-lead ECGs were kept consistent with the original model (Fig. 1 (a1 and b1)).

C. VALIDATION USING THE CLINICAL SURFACE ECGS

The modified refined MI torso-heart model was simulated to obtain body surface potentials, and the standard 12-lead ECGs were calculated. Ten torso-heart models were simulated, including one normal torso-heart model and nine IMI torso-heart models. The normal torso-heart was implemented by defining a refined MI torso-heart model without an MI region. The nine IMI torso-heart models were modeled by changing the sites and sizes as defined above. Numerical solutions of the body surface potentials were calculated using finite element methods. The simulation processes were carried out in a multi-physical simulation software (COMSOL, Switzerland [16]) with default settings, simulating real physical phenomena by solving partial differential equations based on finite element methods. A simulation of a one-second cardiac activity required approximately 5 hours at a resolution of 1 ms (Intel Core i7-7700 CPU, @3.6 GHz, 8G RAM). The average finite element mesh was 38,472 tetrahedral elements with 84,000 degrees of freedom under default settings, which was the same setting in the original model.

After the body surface potentials were obtained, the BSPMs at different instants were calculated. Then, the standard 12-lead ECGs were extracted, and the features of the QRS complex and ST segment in the ECG signals were classified for MI evaluation. The rule-based method for morphological classification was based on our previous work [17]. To verify the validation of the model, the BSPMs calculated from the 308 measuring points were compared with the BSPMs derived from a clinical dataset. The clinical dataset was the case 4 data from the 2007 PhysioNet/Computers in Cardiology Challenge [18]. The data was measured from an MI patient comprising 352-lead body surface potentials (derived from 120 electrode recordings). From the provided clinical interpretation, the MI locations of the patient included 6 segments: basal anterior (1), mid inferoseptal (9), mid inferior (10), mid inferolateral (10), apical inferior (15) and apex (17), and the centroid segment was apical inferior (15). Then, the BSPMs from case 4 were compared with those from the large apical IMI data. Because the original clinical BSPMs included the neck, shoulders, and lower abdomen regions, a rectangular subfigure containing the same regions in the simulated BSPMs was obtained from the original maps. An irregular body surface ECG calculated from two leads outside the standard 12-lead system was also compared between the two datasets. The first lead was located at the lower left back (blue '∗' in Fig. 4 (a1), (b1)); the second lead was selected from the right upper thorax (red '∗' in Fig. 4 (a1), (b1)). To observe differences in the simulated body surface ECGs between the normal heart model and the MI heart models, the 0.5 s lead II signals from different heart status were compared.

D. EFFECTS OF MI SIZES AND SITES ON THE SIMULATED ECGs

To quantify the effects of infarct sizes and sites on ECG morphology, several characteristic points were considered [19].

The ST segment was included because it is a commonly used feature to evaluate the degree of cardiac ischaemia [20]. The amplitude changes in the QRS complex were also compared with normal ECGs. Although several QRS scoring systems exist, including several assessment parameters for locating infarcts and quantifying infarct size [21], [22], these systems are too complex for clinicians to understand. Therefore, only three characteristic points of the QRS complex were adopted: Q wave peak, R wave peak and S wave peak. The T wave was also included.

To identify the optimal leads that reflect the effects of MIs on simulated ECGs according to different characteristic points, derived standard 12-lead ECGs of these models were processed. Before data procession, the dataset of *normalized variation coefficient* (*NVC*) was constructed by equalizing between 0 and 1 (as shown in (7)), and the *amplitude range*s ($Range_{normal}$) of simulated normal ECGs in each lead were calculated (8). The *NVC*s are parameters defined to evaluate the influence of different types of MI on simulated ECGs. First, the *amplitude change*s (*AC*s) of MI ECGs against normal ECGs were calculated in (9). The *AC*s include 9 data types: 3 sizes at 3 sites, each consisting of 12 results, calculated from standard 12-lead ECGs. Then, the *absolute amplitude change ratio*s (*AACR*s) of each lead was obtained by calculating the absolute value of the quotient of *AC* divided by $Range_{normal}$ in (10). This process ensured that all *AACR* changes from the same lead were consistent, and *AACR* changes from different leads were similar. Thereafter, the *AACR*s of each lead were sorted in descending order, and each *AACR* was matched to an *NVC* by mapping to the approximate value from the *NVC*s. To illustrate the evaluation results, the *NVC*s were mapped to a 3×3 color matrix, representing the 3 sizes and 3 sites of MIs. Each color was different shades of grey between white and black according to the value of *NVC*. This colour map can represent the degree of effect of different MIs on ECG morphology in a certain lead. Here, the *NVCs* of five parameters were abbreviated as *NVC_Q*, *NVC_R*, *NVC_S*, *NVC_ST* and *NVC_T*, respectively. The average value of each parameter in each lead were *ANVC_Q*, *ANVC_R*, *ANVC_S*, *ANVC_ST* and *ANVC_T*, respectively.

$$NVC\text{s} = linspace\,(0, 1, 12) \tag{7}$$

$$Range_{normal} = Amplitude_{max} - Amplitude_{min} \tag{8}$$

$$AC\text{s} = Amplitude_{MI} - Amplitude_{Normal} \tag{9}$$

$$AACR\text{s} = abs(AC\text{s}/Range_{normal}) \tag{10}$$

E. COMPARISON BETWEEN CLINICAL AND MODEL DATA

To quantify the similarities between two BSPMs at the same instant, the structural similarity (*SSIM*) index was introduced. Based on the assumption that the human visual system is highly adapted for extracting structural information, the *SSIM* can provide a good approximation for perceived image quality from three aspects between two non-negative signals $\boldsymbol{x}$ and $\boldsymbol{y}$: luminance $l(\boldsymbol{x},\boldsymbol{y})$, contrast $c(\boldsymbol{x},\boldsymbol{y})$, and structure$s(\boldsymbol{x},\boldsymbol{y})$. These indices were defined as follows:

$$l\,(x, y) = (2\mu_x\mu_y + C_1)/\left(\mu_x^2 + \mu_y^2 + C_1\right) \tag{11}$$

$$c\,(x, y) = (2\sigma_x\sigma_y + C_2)/\left(\sigma_x^2 + \sigma_y^2 + C_2\right) \tag{12}$$

$$s\,(x, y) = (\sigma_{xy} + C_3)/\left(\sigma_x\sigma_y + C_3\right) \tag{13}$$

where $\mu_{\boldsymbol{x}}$ and $\mu_{\boldsymbol{y}}$ represent the means of the original and coded images; $\sigma_{\boldsymbol{x}}$ and $\sigma_{\boldsymbol{y}}$ represent the standard deviations of each of the signals; $\sigma_{\boldsymbol{xy}}$ is the covariance of the two photos; $C_1 = (K_1L)^2$, $C_2 = (K_2L)^2$, and $C_3 = C_2/2$ are small constants; L is the dynamic range of the pixel values, i.e., $L = 2^8 = 256$ for an 8-bit greyscale image, and $K_1 \ll 1$ and $K_2 \ll 1$ are scalar constants with default values 0.01 and 0.03, respectively. The constants C_1, C_2, and C_3 ensure stability when the denominator approaches zero. Combining the three terms, the common form of *SSIM* is as follows:

$$SSIM\,(x, y) = [l\,(x, y)]\,[c\,(x, y)]\,[s\,(x, y)] \tag{14}$$

The metric of this formulation ensures that $SSIM(\boldsymbol{x},\boldsymbol{y})\leq 1$ and a unique maximum $SSIM(\boldsymbol{x},\boldsymbol{y})=1$ if and only if $\boldsymbol{x}=\boldsymbol{y}$. Finally, the mean *SSIM* (*MSSIM*) index was used to evaluate the overall image quality as follows:

$$MSSIM\,(X, Y) = \frac{1}{M}\sum_{i=1}^{M} SSIM\,(x_i, y_i) \tag{15}$$

where $\boldsymbol{X}$ and $\boldsymbol{Y}$ are the reference and distorted images, respectively; $\boldsymbol{x_i}$ and $\boldsymbol{y_i}$ are the image contents at the ith local window; and M is the number of local windows of the image.

III. EXPERIMENTS AND RESULTS

A. ECG COMPARISON BETWEEN CLINICAL AND MODEL DATA

Fig. 4 shows instantaneous potential maps during the cardiac cycle from clinical data and simulated results. Fig. 4 (a1) and (b1) are the BSPMs representing the instant at the end of atrial depolarization. In clinical BSPMs (Fig. 4 (a1)), the potential minimum was found near the left mammary area, whereas the potential maximum was at the lower region of torso. Similarly, the potential minimum was located at the right sternal area in simulated maps, and the potential maximum occurred at the lower part of left thoracic wall (Fig. 4 (b1)). At the onset of ventricular repolarization (Fig. 4 (a2), (b2)), the potential maximum was observed at the left thoracic wall in two maps, and the location of the potential minimum was concentrated on the left lateral wall of the torso. The BSPMs all showed a clear bipolar distribution, whereas the clinical BSPMs were somewhat chaotic compared with the simulated BSPMs. This may be due to the presence of multiple infarcted regions in the ventricular wall. However, the simulated maps remained relatively similar to the clinical maps. The potential values of the simulated maps were ten times greater than those of the clinical maps because the simulated potentials were potential values relative to V_{GND}, whereas the clinical potentials were relative to ground. As a result, the distribution of simulated potential was denser than that of the clinical

potential, and the simulated potential values were greater than the clinical potential values. However, the *MSSIM*s between the clinical and simulated BSPMs at two instants shown in Fig. 4 were 0.739 and 0.712, respectively, indicating the simulated potential differences were similar to clinical potential differences, and the distribution tendency was consistent.

To further validate the model, we defined the difference of the potential at the red '∗' and the potential at the blue '∗' in Fig. 4 as irECG and compared the irECGs between simulated results and clinical data at different instants of a cardiac cycle (Fig. 5). Overall, the amplitude of the simulated T wave was smaller than that of the clinical observation, and the position of the simulated T wave was inconsistent to that of the clinical observation (Fig. 5 (a)). This may be due to the anamorphic settings of ventricular conductivity, wide regions of Purkinje fibers and initial values for ventricular extracellular potential and ventricular intracellular potential. Additionally, slight fluctuations in the PR interval may be caused by the cubic settings of the atrial septum, atrioventricular node and His bundle. However, from Fig. 5 (b), the change tendency of the simulated amplitudes at different cardiac instants were similar to those from the clinical data. Moreover, as shown in the simulated ECG and action potentials in Fig. 6, the T-wave in the ECG of the original model was also abnormal compared with the real recorded ECG, whereas the QRS complexes were similar to the real complexes. Because the aim of this paper was to investigate the effects of MI sizes and sites on simulated ECGs using an MI-region-refined torso-heart model, rather than to develop/modify a model, we ignored the abnormal depolarization phase, which is beyond the expectations of the FitzHugh-Nagumo model. Although there are some shape defects on the simulated ECG, this can still reflect the cardiac electrical activities. These

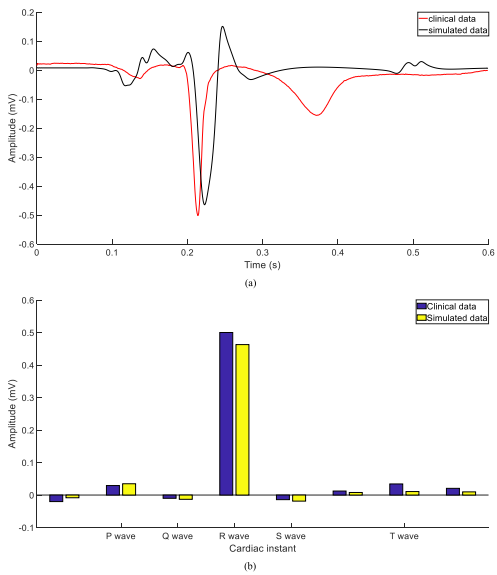

FIGURE 5. Comparison of an irregular body surface ECG between simulated results and clinical data at different instants of a cardiac cycle.

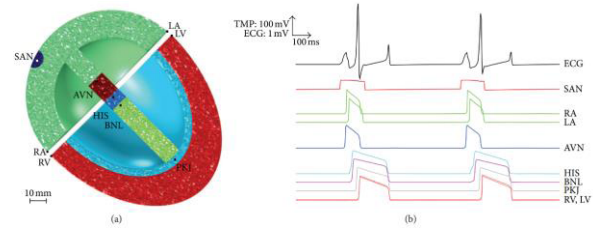

FIGURE 6. Simulation of normal electrical activity. (a) Frontal plane cross section midway through the heart with the probe locations (black dots) positioned throughout the myocardium according to sinoatrial node, right atria, left atria, atrioventricular node, His bundle, bundle branches, Purkinje fibers, right ventricle, and left ventricle. (b) Simulated lead II ECG waveform and the transmembrane action potentials at the probe positions [13].

defects do not influence the comparisons between different MIs and a normal heart because the defective settings exist in all cases. In general, although there are some shape defects on the simulated irregular body surface ECG, the ECG can still reflect the cardiac electrical activities. This model can provide theoretical signals for investigating different normal and pathological heart conditions.

Fig. 7 shows the lead II, III and aVF ECGs of three sizes of MIs at the apical inferior site. The normal ECGs were similar to the MI ECGs (except the T wave). The amplitudes of the Q wave, R wave and S wave from the MI heart differed from the normal ECG, whereas the ST segment and the T wave of the pathological ECG were elevated. Although some of the features were observable, a quantitative investigation of the

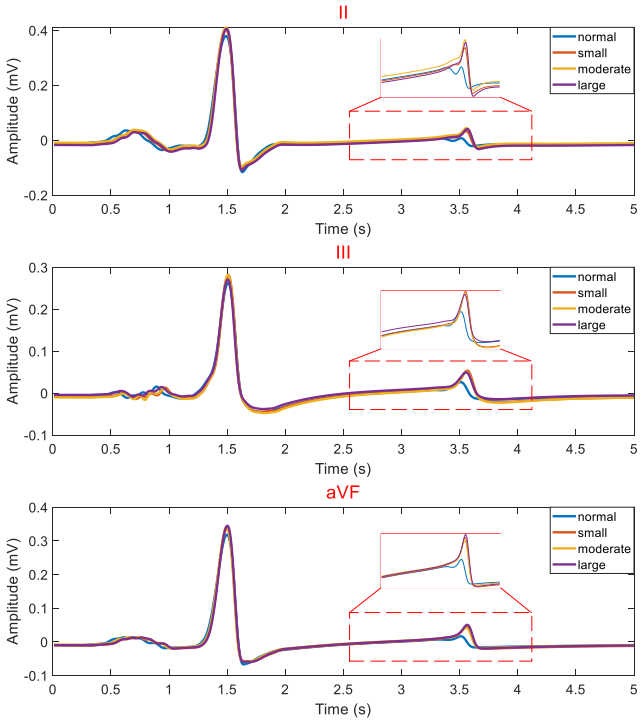

FIGURE 7. Comparison of II, III and aVF lead signals between a normal heart and MIs at apical inferior site.

relationship between the ECG morphology and MI sizes and sites would be required.

B. EFFECT OF THE STIMULATED MI ON ECGs

1) QRS COMPLEX

Fig. 8 illustrates the evaluation results of the R wave (*NVC_R*s), and the *ANVC_R* of each sub-figure (the name of each lead is shown at the bottom of each sub-figure). Lead V6 was the most obvious lead susceptible to MI at the basal site: the average *NVC_R*at this site was 0.73. When the MI was at the middle site, the largest average *NVC_R* was 0.79 in lead V3. At the apical site, the most observable change in the R wave was in lead V4, and the average *NVC_R* was 0.82. However, the small size MI had more obvious effects on simulated ECGs in lead V5 (the average *NVC_R* was 0.73). The largest average *NVC_R* of middle size MI was 0.79 in lead V4, and was 0.64 in leads aVR, V1 and V2 for large size MI. The largest *ANVC_R* was 0.61 in lead V2, i.e., the R wave in this lead was more easily affected than the other leads. The maps of leads V4 and V6 were nearly complementary, indicating that MI sizes and sites can be evaluated with these two leads.

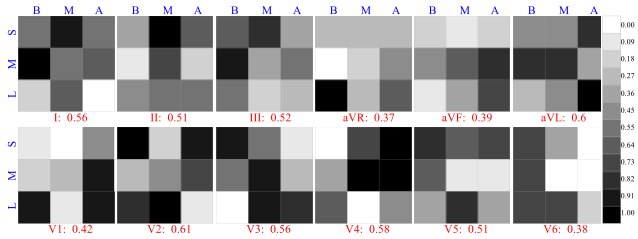

FIGURE 8. ***NVC_R*s for R wave evaluation. B, M and A are the abbreviations of MI site: basal, middle and apical, respectively; S, M and L represent MI size: small, moderate and large, respectively.**

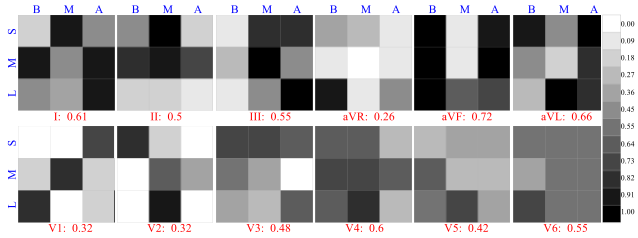

FIGURE 9. ***NVC_Q*s for Q wave evaluation. B, M and A are the abbreviations of MI site: basal, middle and apical, respectively; S, M and L represent MI size: small, moderate and large, respectively.**

The evaluation results of Q wave (*NVC_Q*s) are shown in Fig. 9. At the basal site, the *NVC_Q*s were 1.00 in lead aVF for the three MI sizes. The largest average *NVC_Q* was 0.76 in lead III at the middle site, and 0.88 in lead aVF and aVL at the apical site. When the MI expanded from the small size to the large size, the most observable *NVC_Q*s were 0.79, 0.82 and 0.79 in leads aVL, II and aVF, respectively. The Q wave in lead aVF was the most susceptible lead to MI (*ANVC_Q* in

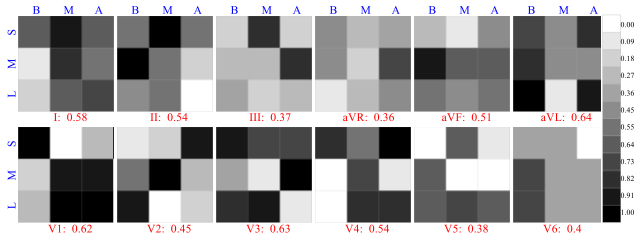

FIGURE 10. ***NVC_S*s for S wave evaluation. B, M and A are the abbreviations of MI site: basal, middle and apical, respectively; S, M and L represent MI size: small, moderate and large, respectively.**

this lead was largest at 0.72). The effect of MI on simulated ECGs in lead V1 was clear.

From Fig. 10, the obvious changes of MI at the basal site was in lead aVL (the average *NVC_S* in this lead was 0.85). The average *NVC_S* in lead I was 0.79 at the middle site, and 0.73 in leads aVL and V1 at the apical site. The largest average *NVC_S* in leads V3 and V4 was 0.79 for the small size MI, 0.73 in lead aVF for the moderate size MI, and 0.76 in lead V1 for the large size MI. The most obvious lead that reflected the influence of MI on the S wave was aVL (the *ANVC_S* was 0.64). Similar to *NVC_Q*s in lead V1, the *NVC_S*s in lead V2 also clearly reflected the effect of MI on simulated ECGs.

2) ST SEGMENT

As shown in Fig. 11, the *NVC_ST*s at the basal site were all 0.73 in lead V6, resulting in the largest average *NVC_ST* at this site (0.73). When the lesion moved to the middle site, the most obvious ST segment changes occurred in lead II, and the average *NVC_ST* was 0.70. At the apical site, the largest *NVC_ST* was 0.82 in lead V2. From the aspect of MI size, the most observable influence of small size MI on simulated ECGs was in lead V3, and the average *NVC_ST* was 0.73. As the lesion expanded to moderate size, the MI affected lead aVF, leading to an average *NVC_ST* of up to 0.91. However, lead V1 was the most susceptible lead to large size MI (the average *NVC_ST* reached 0.70). The largest *ANVC_ST* in leads III and aVF were both 0.61, although the *NVC_ST* did not have the same distribution in these leads. These results indicate that these two leads can be used to evaluate the influence of MI on simulated body surface ECGs.

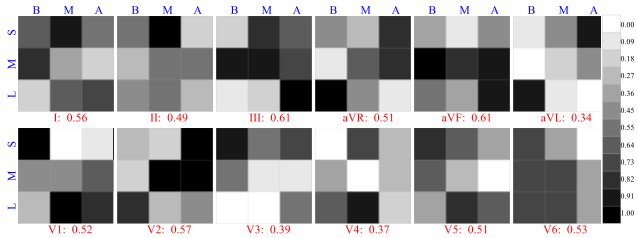

FIGURE 11. ***NVC_ST*s for ST segment evaluation. B, M and A are the abbreviations of MI site: basal, middle and apical, respectively; S, M and L represent MI size: small, moderate and large, respectively.**

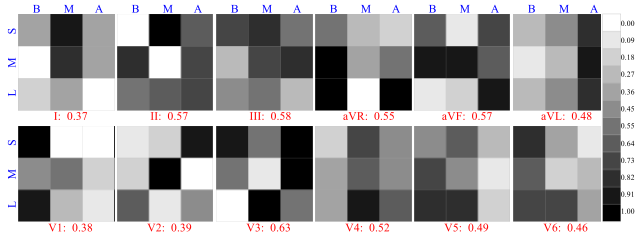

FIGURE 12. ***NVC_Ts*** **for T wave evaluation. B, M and A are the abbreviations of MI site: basal, middle and apical, respectively; S, M and L represent MI size: small, moderate and large, respectively.**

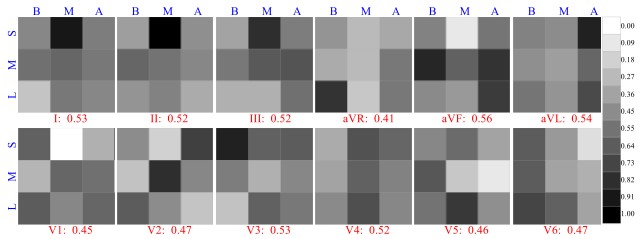

FIGURE 13. **The average** ***NVC*****s for five evaluation parameters. B, M and A are the abbreviations of MI site: basal, middle and apical, respectively; S, M and L represent MI size: small, moderate and large, respectively.**

3) T WAVE

Fig. 12 shows the evaluation results of the T wave (*NVC_T*s). At the basal site, the largest average *NVC_T* was 0.85 in lead aVR. When the MI located at the middle site, the largest average *NVC_T* was 0.70 in leads I and III, indicating these two leads reflected the influence of MI on ECGs. Similarly, the largest average *NVC_T* was also 0.85 when the MI was at apical site. However, it is 0.82 in the small size and moderate size MIs in leads aVF and V3. Lead aVF reflected the effect of large size MI on ECGs (the average *NVC_T* was 0.67). The largest *ANVC_T* comes from lead III (0.58), indicating the most obvious influence of MI on the T wave was in this lead. The influences of large size MI at the basal site, moderate size MI at the middle site and small size MI at the apical site were obvious in lead V2. This indicated that the simulated body surface ECGs in this lead were susceptible to the MIs of these cases.

4) AVERAGE RESULTS FOR THE FIVE CHARACTERISTICS

The above results show that the MI has obvious influences on the five parameters in different leads, indicating that the leads that reflected the effects of MIs on ECGs varied with the characteristic points. The average *NVC*s of these five parameters were calculated and are illustrated in Fig. 13. The obvious lead that reflected the effects of MI at the basal site on ECGs was lead V6 (the average *NVC* was 0.67). Leads I and II showed superiority in reflecting the influence of MIs at the middle site on ECGs (the average *NVC*s were all 0.68). When the MI was located at the apical site, the largest average *NVC* (0.73) occurred in lead aVL. For small size MIs, the MIs affected lead V3 (the largest average *NVC* was 0.71). The most observable influence of middle size MIs on simulated ECGs was in lead aVF (the average *NVC* was 0.76). However, lead V5 was the most susceptible lead to large size MIs (the average *NVC* was 0.59). The largest *ANVC*was from lead aVF (0.56). This indicated that lead aVF was the most obvious lead that reflected the influence of MIs on simulated ECGs among these five characteristic points. Only the *NVC* of small size MIs at the middle site in lead V1 remained at 0.00 after the average of five parameters, indicating that small size MIs had no influence on simulated ECGs in lead V1 at this site. However, the *NVC* of small size MIs at the middle site in lead II was 1.00 after averaging the five parameters, i.e., the effect of small size MIs was obvious on all five characteristic points at this site.

IV. DISCUSSION

In the current study, a refined MI torso-heart model was proposed to evaluate the effect of IMI on simulated body surface ECGs.

The refined MI torso-heart model was modified from a simplified three-dimensional cardiac bidomain model by changing the MI sites and sizes. An additional 308 body surface potential measuring points were added to validate the model. The simulated BSPMs obtained from the model were compared with the BSPMs from an MI patient. The body surface potentials were directly computed from the bidomain finite element method model, rather than calculating the torso surface potential distributions using additional multiple dipole method [4], [23]. The simulated BSPMs were similar to the potential distributions of the clinical data around the anatomical range of heart. The maps represented bipolarity, and the negative potentials always surrounded the positive potentials. The simulated BSPMs were similar to clinical data, and the dipolar potential distribution trend during the cardiac cycle was consistent with clinical observations [24]. The amplitudes of simulated results at different cardiac instants of an irECG were similar to those of clinical cases. Additionally, the simulated ECG morphology in lead II was consistent with the clinical results (except for the T wave). These results reflected detailed changes during the expansion of lesions at different sites. Especially, the changes in the ST segment depression and T wave inversion were in accordance with the clinical criteria for the diagnosis of MI [25].

To evaluate the effect of IMI on simulated body surface ECGs, the *NVC_Q*, *NVC_R*, *NVC_S*, *NVC_ST* and *NVC_T* were used. The obvious influences of MI on the Q wave, R wave, S wave, ST segment and T wave were observed in leads aVF, V2, aVL, III/aVF and III, respectively. The maximum average *ANVC* for the five evaluation parameters was 0.56 in lead aVF (Fig. 13). The most obvious influence of MI on body surface ECGs was in lead aVF, which agreed with prior study results [26]. At the basal site, the most obvious influence of MI was on the Q wave in lead aVF, which agreed with clinical observations of the bundle branch block [27]. The R wave in lead V3 and the S wave in lead V1 showed superiority in reflecting the influence of MI at the middle site on ECGs, which indicated left ventricular hypertrophy [28].

Leads aVF and aVL reflected the effects of MI at the apical site on the Q wave. For small size MIs, obvious influences on the T wave in lead V3 were observed, which was an important diagnostic criterion for the left anterior descending artery or the left circumflex artery [29]. Moderate size MIs had significant influence on the ST segment in lead aVF, as observed in acute inferior wall MIs [26]. Large size MIs also showed obvious influence on the Q wave in lead aVF.

This study had certain limitations. First, other simulations and conditions should be used to optimize the model for more accurate BSPMs, such as considering myocardial anisotropy or basing the geometry of the model on CT/MRI data. Second, more precise changes in ECG morphology should be studied on more precise torso geometries and anisotropic conductivities. Finally, more experiments on MI patients should be conducted to confirm the clinical usefulness of the method.

V. CONCLUSION

In this study, a refined MI torso-heart model was proposed to evaluate the effect of IMI on simulated body surface ECGs. The comparison of BSPMs between the simulated and clinical data, derived from the case 4 data of the 2007 PhysioNet/Computers in Cardiology Challenge, validated this model. The results showed that lead aVF was the most obvious lead that reflected the influence of IMI on body surface ECGs. The sizes and sites of IMI showed that different leads reflected changes to body surface ECGs; these results agreed with clinical observations. We conclude that the modified refined MI torso-heart model provides an alternative tool for quantifying the effect of IMI on a torso-heart model-based body surface ECGs and offers a lead optimization method for ECG detection under specific circumstances, such as wearable conditions.

APPENDIX

Abbreviations are highlighted in TABLE 2.

TABLE 2. Abbreviations section.

Abbreviations	Description
MI	myocardial infarction
ECG	electrocardiogram
BSPM	body surface potential map
IMI	inferior MI
NVC_x	normalized variation coefficient, and x represents five parameters
$\text{Range}_{\text{normal}}$	amplitude ranges of normal model
AC	amplitude change of MI ECG
AACR	absolute amplitude change ratio
ANVC_x	average value of NVC, and x represents five parameters
SSIM	structural similarity index for two pictures
MSSIM	mean value of SSIM

REFERENCES

[1] *Hearts: Technical Package for Cardiovascular Disease Management in Primary Health Care*, World Health Org., Geneva, Switzerland, 2016, pp. 1–73.

[2] W. W. Chen *et al.*, "China cardiovascular diseases report 2015: A summary," *J. Geriatric Cardiol.*, vol. 14, no. 1, pp. 1–10, 2017.

[3] Z. Sankari and H. Adeli, "HeartSaver: A mobile cardiac monitoring system for auto-detection of atrial fibrillation, myocardial infarction, and atrioventricular block," *Comput. Biol. Med.*, vol. 41, no. 4, pp. 211–220, 2011.

[4] S. Giffard-Roisin *et al.*, "Noninvasive personalization of a cardiac electrophysiology model from body surface potential mapping," *IEEE Trans. Biomed. Eng.*, vol. 64, no. 9, pp. 2206–2218, Sep. 2017.

[5] B. Yao, R. Zhu, and H. Yang, "Characterizing the location and extent of myocardial infarctions with inverse ecg modeling and spatiotemporal regularization," *IEEE J. Biomed. Health Inform.*, vol. 22, no. 5, pp. 1445–1455, Sep. 2018.

[6] C. S. Henriquez, "A brief history of tissue models for cardiac electrophysiology," *IEEE Trans. Biomed. Eng.*, vol. 61, no. 5, pp. 1457–1465, May 2014.

[7] C. Corrado *et al.*, "Personalized models of human atrial electrophysiology derived from endocardial electrograms," *IEEE Trans. Biomed. Eng.*, vol. 64, no. 4, pp. 735–742, Apr. 2017.

[8] F. A. Beltrán-Molina, J. Requena-Carrión, F. Alonso-Atienza, and N. Zemzemi, "An analytical model for the effects of the spatial resolution of electrode systems on the spectrum of cardiac signals," *IEEE Access*, vol. 5, pp. 18488–18497, 2017.

[9] H. J. Arevalo *et al.*, "Arrhythmia risk stratification of patients after myocardial infarction using personalized heart models," *Nature Commun.*, vol. 7, no. 1, 2016, Art. no. 11437.

[10] R. R. Aliev and A. V. Panfilov, "A simple two-variable model of cardiac excitation," *Chaos, Solitons Fractals*, vol. 7, no. 3, pp. 293–301, 1996.

[11] J. M. Ferrero J. B. Trénor, B. Rodríguez, and J. Sáiz, "Electrical activity and reentry during acute regional myocardial ischemia: Insights from simulations," *Int. J. Bifurcation Chaos*, vol. 13, no. 12, pp. 3703–3715, 2003.

[12] S. Sovilj, R. Magjarević, N. Lovell, and S. Dokos, "Realistic 3D bidomain model of whole heart electrical activity and ECG generation," in *Proc. Comput. Cardiol.*, Sep. 2013, pp. 377–380.

[13] S. Sovilj, R. Magjarević, N. H. Lovell, and S. Dokos, "A simplified 3D model of whole heart electrical activity and 12-lead ECG generation," *Comput. Math. Methods Med.*, vol. 2013, Mar. 2013, Art. no. 134208.

[14] R. H. Selvester, D. G. Strauss, and G. S. Wagner, "Myocardial infarction," in *Comprehensive Electrocardiology*. London, U.K.: Springer, 2010, pp. 651–746.

[15] D. C. Sevilla *et al.*, "Anatomic validation of electrocardiographic estimation of the size of acute or healed myocardial infarcts," *Amer. J. Cardiol.*, vol. 65, no. 20, pp. 1301–1307, 1990.

[16] C. Multiphysics, "Comsol multiphysics user guide (version 4.3 a)," COMSOL AB, Stockholm, Sweden, Tech. Rep. CM020002, 2012.

[17] M. Xu, S. Wei, X. Qin, Y. Zhang, and C. Liu, "Rule-based method for morphological classification of ST segment in ECG signals," *J. Med. Biol. Eng.*, vol. 35, no. 6, pp. 816–823, 2015.

[18] F. Dawoud, G. S. Wagner, G. Moody, and B. M. Horáček, "Using inverse electrocardiography to image myocardial infarction—Reflecting on the 2007 physionet/computers in cardiology challenge," *J. Electrocardiology*, vol. 41, no. 6, pp. 630–635, 2008.

[19] U. Iqbal, T. Y. Wah, M. H. U. Rehman, and M. Qurat-Ul-Ain, "Usage of model driven environment for the classification of ECG features: A systematic review," *IEEE Access*, vol. 6, pp. 23120–23136, 2018.

[20] J. Garcia, L. Sornmo, S. Olmos, and P. Laguna, "Automatic detection of ST-T complex changes on the ECG using filtered RMS difference series: Application to ambulatory ischemia monitoring," *IEEE Trans. Biomed. Eng.*, vol. 47, no. 9, pp. 1195–1201, Sep. 2000.

[21] V. Bono *et al.*, "Development of an automated updated selvester QRS scoring system using SWT-based QRS fractionation detection and classification," *IEEE Trans. Biomed. Eng.*, vol. 18, no. 1, pp. 193–204, Jan. 2014.

[22] G. Goovaerts, S. Padhy, B. Vandenberk, C. Varon, R. Willems, and S. V. Huffel, "A machine learning approach for detection and quantification of QRS fragmentation," *IEEE J. Biomed. Health Inform.*, To be published. 2018.

[23] D. Wei, O. Okazaki, K. Harumi, E. Harasawa, and H. Hosaka, "Comparative simulation of excitation and body surface electrocardiogram with isotropic and anisotropic computer heart models," *IEEE Trans. Biomed. Eng.*, vol. 42, no. 4, pp. 343–357, Apr. 1995.

[24] G. Yang, J. Chen, L. Xie, J. Mao, H. Tenhunen, and L.-R. Zheng, "A hybrid low power biopatch for body surface potential measurement," *IEEE J. Biomed. Health Inform.*, vol. 17, no. 3, pp. 591–599, May 2013.

[25] K. Thygesen *et al.*, "Third universal definition of myocardial infarction," *Ciruculation*, vol. 126, no. 16, pp. 2020–2035, 2012.
[26] S. Sadanandan *et al.*, "Clinical and angiographic characteristics of patients with combined anterior and inferior ST-segment elevation on the initial electrocardiogram during acute myocardial infarction," *Amer. Heart J.*, vol. 146, no. 4, pp. 653–661, 2003.
[27] H. Hod, U. Goldbourt, and S. Behar, "Bundle branch block in acute Q wave inferior wall myocardial infarction: A high risk subgroup of inferior myocardial infarction patients," *Eur. Heart J.*, vol. 16, no. 4, pp. 471–477, 1995.
[28] I. A. Khan and I. S. Shaw, "Pseudo myocardial infarction and pseudo ventricular hypertrophy ECG patterns in Wolff-parkinson-white syndrome," *Amer. J. Emergency Med.*, vol. 18, no. 7, pp. 802–806, 2000.
[29] N. Safdarian, N. J. Dabanloo, and G. Attarodi, "A new pattern recognition method for detection and localization of myocardial infarction using T-wave integral and total integral as extracted features from one cycle of ECG signal," *J. Biomed. Sci. Eng.*, vol. 7, pp. 818–824, Aug. 2014.

ZHIPENG CAI received the B.S. degree in measurement and control technology and instrument from the School of Mechanical Engineering, Jiangsu University, Zhenjiang, China, in 2013, and the M.S. degree from the School of Instrument Science and Engineering, Southeast University, Nanjing, China, in 2015, where he is currently pursuing the Ph.D. degree in instrument science and technology. His current research interests include bio-signal processing, body sensor networks, and cardiac electrophysiology simulation.

JIANQING LI received the B.S. and M.S. degrees in automatic technology from the School of Instrument Science and Engineering, Southeast University, China, in 1986 and 1992, respectively, and the Ph.D. degree in measurement technology and instruments from Southeast University. He is currently a Professor and a Vice Present of the School of Basic Medical Sciences, Nanjing Medical University, China. He is also a Professor with the School of Instrument Science and Engineering, Southeast University, China. His research interests include mHealth and wireless networks.

KAN LUO received the M.S. degree from the Chongqing University of Technology, Chongqing, China, in 2011, and the Ph.D. degree in instrument science and technology with Southeast University, China, in 2015. He is currently with the School of Information Science and Engineering, Fujian University of Technology, Fuzhou, China. His current research interests include bio-signal processing, body sensor networks, and machine learning.

BOR-SHYH LIN received the B.S. degree from the Electrical and Control Engineering Department, National Chiao Tung University, Hsinchu, Taiwan, in 1997, and the M.S. and Ph.D. degrees from the Institute of Electrical Engineering, National Taiwan University, Taipei, Taiwan, in 1999 and 2006, respectively, where he is currently with the Institute of Imaging and Biomedical Photonics. His current research interests include medical informatics and biomedical signal processing.

ZHIGANG WANG received the B.S. degree in electronic engineering and the M.S. degree (Hons.) in biomedical engineering and instrumentation from Chongqing University, Chongqing, China, in 1983 and 1986, respectively, and the Ph.D. degree in biomedical engineering from the University of Dundee, Dundee, U.K., in 2005.

He was an Associate Professor with Chongqing University. In 1991, he was a Visiting Scholar with King's College London, U.K. In 1998, he was a Research Fellow with the University of Dundee, where he is currently a Lead Electronic Engineer with the Surgical Technology Group, Institute of Medical Science and Technology (IMSaT). His research expertise is medical instrumentation. He has authored or co-authored more than 40 research articles published in international journals and conferences. He holds four international patents in medical devices. His current research interests include minimal invasive surgical technology and noninvasive medical technology.

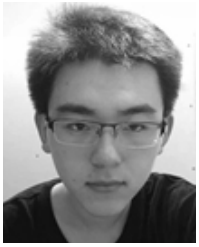

XIANGYU ZHANG received the B.S. degree in measurement and control technology and instrument from the School of Mechanical Engineering, Southwest Jiaotong University, Chengdu, China, in 2014. He is currently pursuing the Ph.D. degree in instrument science and technology with Southeast University, Nanjing, China. His current research interests include deep learning, bio-signal processing, and body sensor networks.

CHENGYU LIU received the B.S. and Ph.D. degrees in biomedical engineering from Shandong University, China, in 2005 and 2010, respectively.

He has completed the postdoctoral trainings at Shandong University, China, from 2010 to 2013, Newcastle University, U.K., from 2013 to 2014, and Emory University, USA, from 2015 to 2017. He is currently a Professor with the School of Instrument Science and Engineering, Southeast University, Nanjing, China. He is also the Director of the Southeast-Lenovo Wearable Heart-Sleep-Emotion Intelligent Monitoring Lab. He was a PI on more than ten awarded grants. He has published more than 100 papers, eight chapters in books, and 15 invention patents. His research interests include mHealth and intelligent monitoring, machine learning and big data processing for cardiovascular signals, device development for CADs, and sleep and emotion monitoring. He is currently a Federation Journal Committee Member of the International Federation for Medical and Biological Engineering (IFMBE).